SolarPede: a stick-and-slip, light-powered, Mobile micro-crawler

Ruoshi Zhang, Jordan F. Klotz,
Danming Wei, Zhong Yang, Andriy
Sherehiy, Mohammad N. Saadatzi & Dan
O. Popa

Journal of Micro-Bio Robotics

ISSN 2194-6418

J Micro-Bio Robot DOI 10.1007/s12213-020-00131-6



Your article is protected by copyright and all rights are held exclusively by Springer-Verlag GmbH Germany, part of Springer Nature. This e-offprint is for personal use only and shall not be self-archived in electronic repositories. If you wish to self-archive your article, please use the accepted manuscript version for posting on your own website. You may further deposit the accepted manuscript version in any repository, provided it is only made publicly available 12 months after official publication or later and provided acknowledgement is given to the original source of publication and a link is inserted to the published article on Springer's website. The link must be accompanied by the following text: "The final publication is available at link.springer.com".



Journal of Micro-Bio Robotics https://doi.org/10.1007/s12213-020-00131-6

RESEARCH PAPER



SolarPede: a stick-and-slip, light-powered, Mobile micro-crawler

Ruoshi Zhang¹ • Jordan F. Klotz¹ • Danming Wei¹ • Zhong Yang¹ • Andriy Sherehiy¹ • Mohammad N. Saadatzi¹ • Dan O. Popa¹

Received: 18 December 2019 / Revised: 2 March 2020 / Accepted: 16 March 2020 © Springer-Verlag GmbH Germany, part of Springer Nature 2020

Abstract

In this paper, we present recent research results aimed at creating mobile microrobotic agents powered by light energy. The SolarPede is a second-generation, cm-scale micro-crawler targeting microfactory applications. The microrobot is equipped with a legged locomotion system and an electronic backpack. This novel microrobot is an advancement in functionality and design over its decade-old predecessor, the ARRIPede, and includes technological advancements such as wireless communication, light power, and omnidirectional mobility on a flat operating surface. The robot "chassis" consists of Micro Electromechanical System (MEMS) electrothermal actuators and micro-assembled vertical legs. Attached to the "chassis" is an electronic backpack realized using custom Printed Circuit Boards and interfaced to the Silicon body by wire-bonding. A simulation model for the SolarPede was created to predict system behavior and dynamic operation, and to serve as a design tool. Finally, the omni-directional locomotion of the SolarPede was experimentally confirmed in a "belly-up" configuration and powered by a solar simulator. A Silicon payload was tracked under optical microscope to measure and verify the motion velocity of 40 µm/s can be achieved by the microrobot in untethered operation with light irradiance equivalent to 8 suns.

Keywords Microrobot · Solar cells · Thermal actuator

1 Introduction

Recent research has explored the possibilities of constructing microfactories that are affordable, flexible, and scalable. One solution towards such goal often incorporates off-the-shelf motorized stages, actuators, and customized metal parts to achieve high precision processing and manufacturing [1–3]. However, these examples have several drawbacks, such as lack of parallel processing capability [3] and difficulty in scaling to lower dimensions [4]. Another solution proposed for next generation microfactories envisioned microrobots, both mobile and fixed [5–7]. Mobile microrobots will be needed to reposition material in the microfactory while being capable of wireless navigation and autonomous task execution [8].

Electronic supplementary material The online version of this article (https://doi.org/10.1007/s12213-020-00131-6) contains supplementary material, which is available to authorized users.

Ruoshi Zhang ruoshi.zhang@louisville.edu

Published online: 21 April 2020

Recent results in creating mobile microrobots for dry environments include cilia-like gated crawlers [9, 10], magnetic levitation [6, 11], piezoresistive stick-and-slip effects [12], and light-powered PZT actuators [13, 14].

The ARRIPede [9, 15] was an untethered, microassembled MEMS microrobot, capable of stick-and-slip operation while powered by an on-board Lithium-Polymer battery. While storing energy on-board for use during operation provides maximum functional flexibility, it is technically challenging to implement due to the unfavorable dimensional scaling of battery power sources. Such arrangement also requires the battery to be disassembled from the microrobot and recharged. Therefore, it is desirable to harvest ambient energy, for instance from light sources such that an onboard battery is not required. The ARRIPede's gait and locomotion methods have been well characterized and accompanied by stick-andslip dynamic models [10, 15]. This early design demonstrated a great payload carrying capacity of 9 g, and non-holonomic mobility characterized by forward-only and large turn radii with speeds in excess of 1 mm/s. However, the operation of this microrobot was seriously limited due to a short battery life (approximately 10 min), a nonholonomic motion dexterity on the operating surface, and the lack of wireless communication for start, stop and feedback control.



¹ University of Louisville, Louisville, KY, USA

In this paper, we design and experimentally validate SolarPede, a solar-powered micro-crawler, that overcomes many of the operational limitations of ARRIPede. Unlike ARRIPede, the SolarPede does not use a battery to store energy in order to reduce weight and complexity of the system, and it was designed to operate in a controlled environment with artificial light that can constantly track its solar cells and provide perpetual power. Microrobot actuation of the SolarPede was accomplished via electrothermal "Chevron" actuator banks, referred to as "thermal actuators" in the paper, and vertically micro-assembled legs, realized with snapfasteners [16]. On SolarPede, the actuators and legs were rearranged in a differential drive configuration to achieve omni-directional, rather than nonholonomic locomotion. An on-board battery is no longer required for SolarPede and was replaced with high-efficiency solar cells to eliminate the need for battery recharging, while balancing microrobot power with solar energy from a solar simulator. The SolarPede's on-board computer is a Bluetooth-enabled 32-bit microcontroller unit, which increases both programming and wireless communication flexibility. Electronic backpack prototypes implementing solar-power harvesting, and gait sequencing control were implemented and experimentally tested. By integrating all subsystems of the SolarPede, we demonstrated a fully untethered, light-driven omnidirectional microrobot operating as a nano positioner on planar surfaces.

A dynamic model was proposed and experimentally validated to predict the microrobot behavior. This model was used as a design tool and to understand the motion characteristics of the microrobot. The scientific contribution of our work consists of the novel leg and gait designs to achieve omnidirectional motion, as well as the methods employed to accomplish microrobot energy balance through leg powermultiplexing, solar energy harvesting, and electronic backpack design.

In contrast to the I-Swarm light-driven microrobots [12], SolarPede's design and form factor allow it to have a much larger payload capacity, utilize off-the-shelf electronic components, and achieve nano-scale precision for operation inside a microfactory. Specifically, the measured weight of the SolarPede is 4 g, while its vertical legs are capable of supporting 9-g payloads [15]. The microrobot's thermal actuators are capable of generating large forces in excess of 50mN [17] and achieve nanometric motion resolution [10]. As a result, the SolarPede specifications are closer to a Scanning Electron Microscope mobile microrobot such as MINIMAN [18]. In this paper, we report on results obtained to date validating that our concept is sound, including controlled operation of our microrobot in "belly-up" conveyor mode. Results suggest that in the near future, a mobile SolarPede can be miniaturized to a cm-scale form factor for crawling operation required in microfactory tasks.

The paper is organized as follows: in Section 2 we describe the SolarPede design and operational principles; Section 3 discusses fabrication and assembly of the MEMS part; in Section 4 we present stick-and-slip model of each leg and overall microrobot motion pattern; Section 5 gives detailed experiment results including power efficiency evaluation, SolarPede motion validation, and system integration test; Section 6 concludes the paper and discusses future work.

2 Microrobot design

The SolarPede microrobot has two major components: an assembled MEMS die and an electronics backpack, with overall footprint of $26 \times 20 \times 6$ mm. The SolarPede is envisioned as a legged micro-crawler consisting of two subsystems, Electronic and MEMS, depicted in Fig. 1 (a). The first subsystem is a MEMS device which serves as the "chassis" and holds the actuated legs of the micro-crawler. The second subsystem is the electronic "backpack" implemented as a pair of printed circuit boards, solar panels and all electronic components necessary for the robot's powered operation. A system level functionality abstraction is shown in Fig. 1 (b).

2.1 The MEMS die and the legs

The "chassis" of SolarPede is a 1cm² MEMS die with 8 thermal actuators [19]. At the end of the thermal actuators' shaft, we included a so-called "Zyvex snap-fastener" [20, 21], which allows a vertical, compliant MEMS leg to assemble perpendicularly into the body of the robot. As indicated in Fig. 2 (b), the Zyvex snap-fastener includes two components: a socket attached to the end of the shaft as a receptor and a plug on the leg. A special end-effector was used to pick up the leg and assemble it into the socket. The electrical interconnects for these actuators are positioned on two edges of the die so that wire bonding can be easily accomplished. The actuator-leg arrangement is shown in Fig. 2 (a), with dimensions chosen to accommodate the Zyvex socket dimensions, and to guarantee significant leg displacements of up to 50 µm. The tip of the leg was rounded in order to mitigate errors in the event of a poor assembly resulting in a tilted leg. If the leg shape was rectangular, the corner of a tilted leg would create undesired off-axis actuation forces and prevent other legs from contacting the operating surface.

Inspired by the mecanum wheels or differential drive arrangements for large mobile robots, we placed the 8 legs in a way that enables omnidirectional motion, as shown in Fig. 2 (a). The die has been split into four identical quadrants; each contains two actuators with opposite diagonal direction of motions. Due to its symmetrical nature, omnidirectional motion can be achieved.



Fig. 1 (a) Side-view illustration of SolarPede's construction. (b) System level functionality abstraction of SolarPede

2.2 Principle of operation

The SolarPede micro-crawler achieves locomotion using stickand-slip effects between the legs and the operating surface, in a manner thoroughly discussed in [10]. By timing the displacement of the legs, a forward gait motion can be obtained for which the velocity is proportional to the amplitude-frequency product of the leg. Unlike the 8-legged nonholonomic design of the ARRIPede [9], the SolarPede contains actuator arrays which can be individually controlled to generate more dexterous maneuvers on the operating surface.

Actuating the eight legs in certain sequences, a combined force can be generated with controlled direction, hence creating directional motions. We use Fig. 3 to explain three sequencing methods that create directional and steering motions, in which (a) to (d) illustrate the simple directional motions aligned with the x and y axes, (e) and (f) illustrate combined forces causing steering motions.

- (1) To generate a combined force on the +y direction as indicated by the red arrow in Fig. 3 (a), actuators 1, 4, 6, 7 are engaged by applying an actuation voltage simultaneously. Then release them by removing the voltage, at the same time, engage actuator 2, 3, 5, 8. Black arrows are used to indicate the combined force for each quadrant. At the moment of the transition, all eight legs are in motion and causing a net force in the +y direction while the lateral directional (±x) forces cancel each other.
- (2) The second sequencing method is similar to (1) but relies on engaging half of the actuators at one time. For

- example, to generate forces in +y direction, engage actuators 1 and 4, release, and engage 2 and 3. Then engage 6 and 7, release, and engage 5 and 8. We will use this method as the preferred leg actuation sequence for our SolarPede, since our on-board power is limited.
- (3) The third method engages each quadrant at one time: engage actuator 1, release, and engage 2; engage 4, release, then engage 3; engage 6, release, then engage 5; engage 7, release, then engage 8, which generates force on +y direction. This method was employed during our early prototype stage [22].

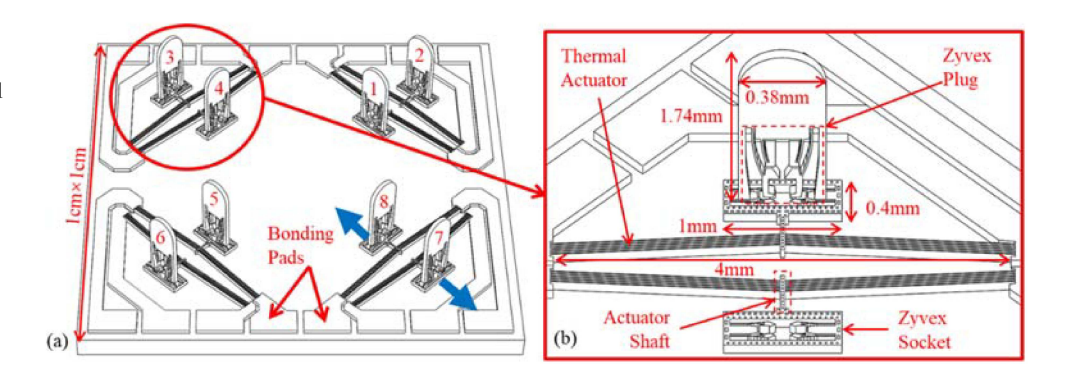
In addition to these methods, engaging one quadrant more often than others could generate steering motion, as indicated in Fig. 3 (e) and (f).

Theoretically, all three methods can be used to create omnidirectional motions. The first method has the highest power requirement since it engages 4 actuators simultaneously, the second method engages two actuators simultaneously and the third engages one at each time. Simulations were carried out in Section 4.2 for method (2), to verify that directions of motion indicated by the arrows, will be achieved.

2.3 Electronics and solar cells

Powering and controlling of the SolarPede is accomplished through an electronic backpack mounted onto the Silicon die. The backpack contains a power board and a control board, as depicted in Fig. 1. On top of SolarPede is the power board

Fig. 2 (a) CAD Model of assembled SolarPede die. (b) Dimension of the leg and thermal actuator, each actuator beam is 10 μm wide and all assembled parts are 100 μm thick





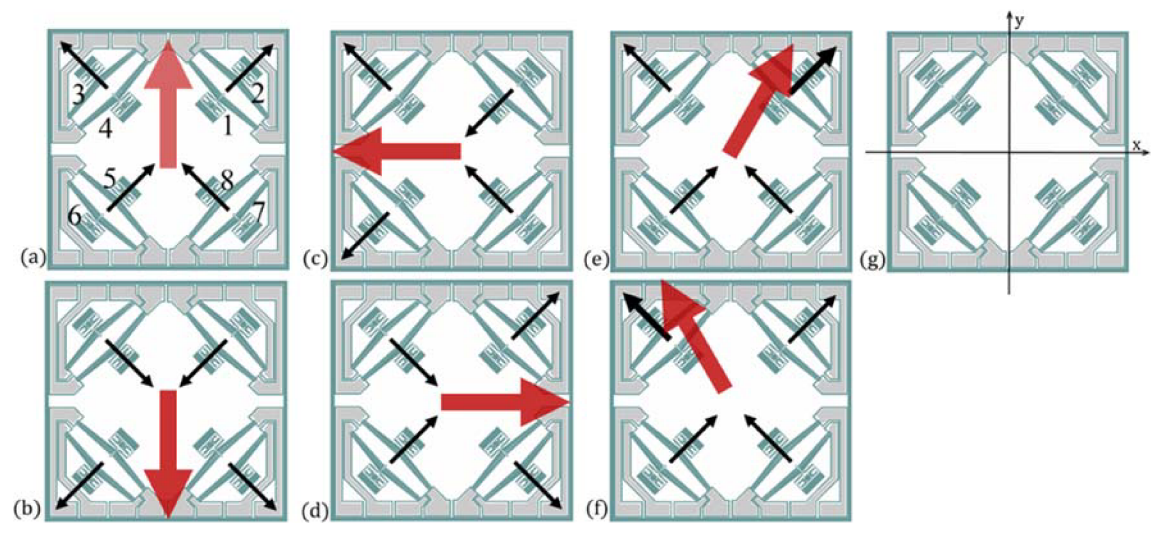


Fig. 3 Theoretical vectors of holonomic motion methodology for SolarPede omnidirectional leg arrangement. Thicker vectors indicate motion performed at higher frequency than other vectors. (a) to (f)

corresponding to up, down, left, right, up-right, and up-left forces. (g) shows the definition of the x and y axes

which accepts artificial light irradiation and converts energy for the microrobot. The power board has two major components: four solar cells in series configuration and a voltage boost converter circuit. The rated voltage of the solar cell is 2.5 V (Spectrolab®, CDO-100), four of them in series generate roughly 10 V under 5 suns irradiance, it is high enough to drive one thermal actuator to create observable displacement. Either used directly or boosted, this voltage is referred to as the "high voltage" in the remainder of this paper. In addition, 2.5 V from the bottom of the four-in-series solar cells is wired out to provide power to the MCU.

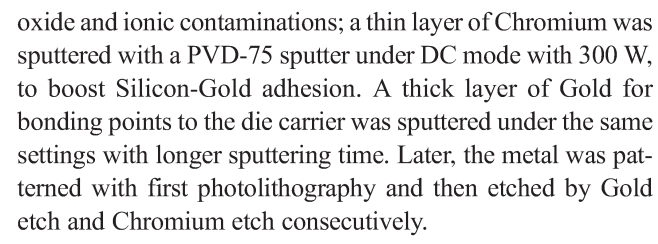
Through wired connection, the high voltage, 2.5 V, and ground are routed onto the control board, which contains a Bluetooth microcontroller unit (MCU) module, BL652 from Laird®, and a MOSFET (ON Semiconductor, NTHD4508N) array. The MCU works in conjunction with the MOSFET array to create the gaiting patterns required for steerable motion of the microrobot. And lastly, the MEMS die is attached to the back of the control board and wire bonded.

3 MEMS fabrication and assembly

3.1 Fabrication

The body and legs of SolarPede are fabricated on a silicon-on-insulator (SOI) wafer with the following parameters: the device layer is N-type with 0.01 to 0.02 Ω -cm resistance, 100 μ m thick device layer and <100> orientation; the buried oxide layer is 2 μ m thick and the handle layer is P-type with larger than 1000 Ω -cm resistance and 500 μ m thickness.

The fabrication follows the standard SOI process. An RCA clean was performed as the first step, to remove any organic,



Deep reactive ion etching (DRIE) was performed with a strong photoresist mask (SPR220–3.0) on the wafer to define the body of the SolarPede. Etching time is derived from experience with the tool and checked under microscope to confirm finishing of etching. Before dicing the wafer, a protective layer of photoresist was spun to prevent debris from damaging or jamming the moving features. After dicing, selected dies were submerged in 49% hydro-fluoric acid to release the moving parts from the wafer surface. Eventually, all released dies were dried by critical point dryer (CPD) to conclude all fabrication processes.

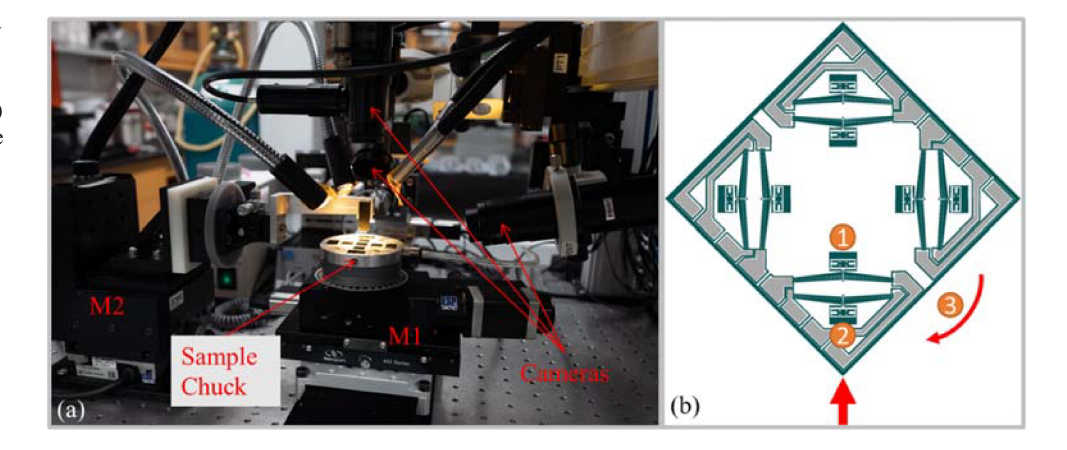
3.2 Assembly

To assemble the legs on the SolarPede base, a custom microassembly system, called NeXus [23], was employed. The NeXus includes two manipulators (M2 holding a microgripper and M1 holding the MEMS die substrate) and three imaging systems as shown in Fig. 4 (a). M1 consists of two motorized linear stages and one motorized rotation stage to realize X-Y- three degrees of freedom (DOFs). M2 consists of motorized X-Y-Z- stages and an extra manual X-Y stage to present 6 DOFs [24].

An end-effector mounted with a micro-jammer is connected to the manual X-Y stage by kinematic base on M2. Figure 4 (a) also shows the three imaging systems that provide views



Fig. 4 (a) NeXus microassembly station. (b) Leg assembly sequence: 1) Assemble the inner leg. 2) Assemble the outer leg. 3) Rotate the sample 90° to assemble another pair of legs



for the assembly processing from vertical, horizonal and side directions. The 45° arrangement of the legs adds a twist in the assembly process; hence the assembly sequence should be carefully planned to avoid conflictions and damages to the structure.

The legs were first picked up by the micro-jammer (M2), and then the M1 manipulator rotates the sample chuck by 45° so that the leg is aligned with the assembly site. As shown in Fig. 4 (b), the leg approaches the assembly site by the red arrow at the bottom, the first leg attaches to the inner site marked as 1, then the second leg was picked up and attached to the outer site marked as 2. After the two legs were attached, UV sensitive epoxy was applied and cured at the joint to increase the mechanical strength. Third, by rotating the sample chuck 90°, this process can be repeated to assemble the next group of legs.

4 Modeling and analysis of the microrobot

In this section, a mathematical model of the microrobot is proposed, in order to analyze and further simulate the motion of the SolarPede prior to its design and fabrication. Simulations help to predict the expected velocity of the microrobot under various design parameters and constraints, including actuator sizes, friction coefficients and robot payloads. Later in this section, by using the model, we also discuss how unbalanced friction forces on the legs will likely affect the motion trajectory of SolarPede, and how the leg gating sequences will result in its motion along specific planar directions.

4.1 Stick and slip model and legs displacement

The SolarPede's motion is caused by breaking the static friction under its feet as well as at the joints in the heating cycle, followed by the whole robot body movement in the cooling cycle. Figure 5 depicts a lumped mass-spring-damper (MSD) model of the robot's leg. In this model, M₁ and M_b are the leg's

mass and the robot body mass, respectively. K represents the stiffness and B is the damping coefficient of the thermal actuator.

In this model, two friction forces combined to resist motion inputs from the thermal actuator: one between the foot and operating surface, f_1 , and another at the joint between the assembled leg and the microrobot body, f_2 . Following Newton's second law of motion, the dynamic equations of such a system can be written as:

$$M_l \ddot{X}_l = -F_a + f_1 + f_2 + K(X_b - X_l) + B(\dot{X}_b - \dot{X}_l) \#$$
 (1)

$$M_b \ddot{X}_b = F_a - f_2 - K(X_b - X_l) - B(\dot{X}_b - \dot{X}_l) \#$$
 (2)

$$f_1 = \mu(M_b + M_l)g\# \tag{3}$$

$$f_2 = \mu M_b g \# \tag{4}$$

Where μ is the coulomb friction coefficient switching between static μ_s and dynamic μ_d in the stick-and-slip phases of leg motion, respectively, F_a is the actuation force generated by the thermal actuator under a certain input voltage of V. X_l and X_b are the corresponding displacements of M_l and M_b .

The value of F_a during actuation cycles can be empirically estimated from steady-state displacement of the thermal actuator according to a first order model:

$$F_a(V, f) = \frac{2NAEsin^2(\theta)}{L} \cdot \frac{\lambda V^2}{1 + s\frac{f}{f_{PW}}} \#$$
 (5)

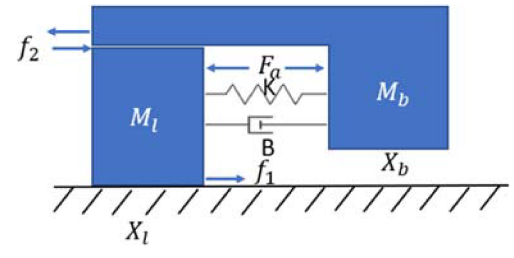


Fig. 5 Mass-spring-damper model of the SolarPede's leg and body



In which N=6 is the number of actuator beams within one thermal actuator, E is the Young's modulus of Silicon, θ is the actuator's beam bending angle, in our case 3.4°, A is the cross-section area of the actuator, V is the input voltage, f is the actuator's resonant frequency, $f_{\rm BW}$ is the actuator's bandwidth, and λ is an empirical constant [25].

Values used to simulate the leg motion were selected from the dimension parameters of the actuator and leg, in particular, K = 185 N/m, $M_l = 0.3 \text{ mg}$, $M_b = 0.25 \text{ g}$, while λ and $f_{\rm BW}$ were estimated from experiments as 0.03 and 50 Hz. Furthermore, assuming the friction coefficients for Silicon-Silicon contact were $\mu_s = 0.4$, and $\mu_d = 0.33$. Our estimated forward velocity of the leg-body model is shown in Fig. 6.

In particular, simulation results indicate that we should expect forward velocities greater than 10 μ m/s for a wide range of frequencies if the actuation voltage is 20 V.

4.2 Body motion analysis

According to the 3 proposed gaiting patterns in Section 2.2, the SolarPede's holonomic motion relies on the combined directional force being applied to the body of the microrobot.

The SolarPede has eight legs in total. Each leg has one DOF, so that at least eight coupled differential equations are needed to fully describe its motion. To simplify this, we consider each quadrant as a single unit that generates a force $\mathbf{F_x}$ along the thermal actuator centerline, which in the ideal case passes through the SolarPede center of mass, as shown in Fig. 7. Each force originates from the center of the two actuators, and they are described by the one-dimensional model we have derived. Notice that each of these $\mathbf{F_x}$ is a combined force. For example, $\mathbf{F_1}$ shown in Fig. 7 is the force generated at the moment of actuator 1 retracking while actuator 2 is engaging. If this sequence reverses, the direction of $\mathbf{F_1}$ also reverses.

The microrobot's body experiences a total force of:

$$\sum F = F_1 + F_2 + F_3 + F_4 \#$$
 (6)

From (6), if the magnitude of the four vectors are different, then directional motion can be imparted on the microrobot.

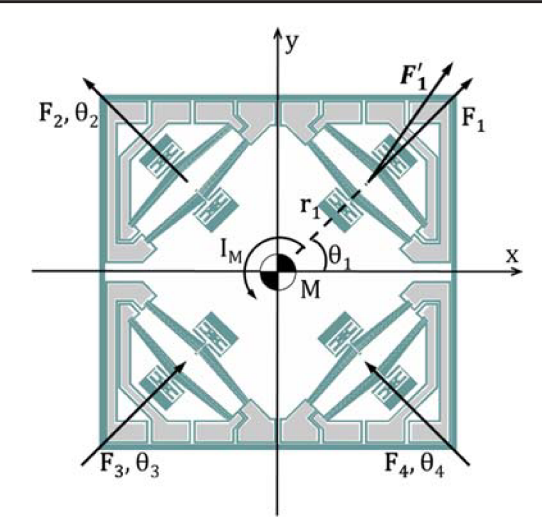


Fig. 7 SolarPede body motion analysis

Many factors contribute to this imbalance, including controllable effects (magnitude, frequency) and uncontrollable effects, for instance, different leg-surface contact condition, misalignment during leg assembly process, or tilted legs.

Since the SolarPede actuator placement is symmetric, the actuation force can be seen directly applied at the geometric center in this model and hence can be combined into two, such as F_1 and F_2 . By assigning different friction constants relating to F_1 and F_2 , we can simulate the motion pattern when the legs experience different friction, as results shown in Fig. 8 (a). In the plot, μ_s and μ_d represent static and dynamic friction constants respectively, and the l and r subscript represent force on the left or right.

As the simulation indicates, if the friction constant on the left and right are the same, a straight trajectory can be expected, otherwise sideway motion or drifting can be expected.

The proposed gaiting method 2 described in Section 2.2 were simulated with our model and the resulting directions of motion are shown in Fig. 8 (b). In this simulation, we combined the forces generated by actuators located in adjacent quarters to generate resultant forces R_i , $i = 1 \sim 4$. The simulation was run for 1 min, under 10 Hz and 30 V. The maximum displacements were 2 mm, indicating a velocity of 33.3 μ m/s. As expected, these resultant motions align with desired

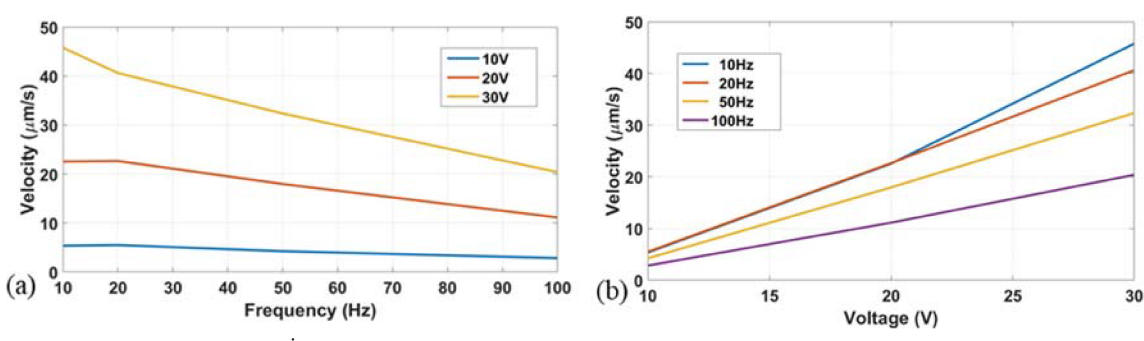


Fig. 6 Plots of microrobot body velocity X_b vs. (a) leg actuation frequency, and (b) voltage



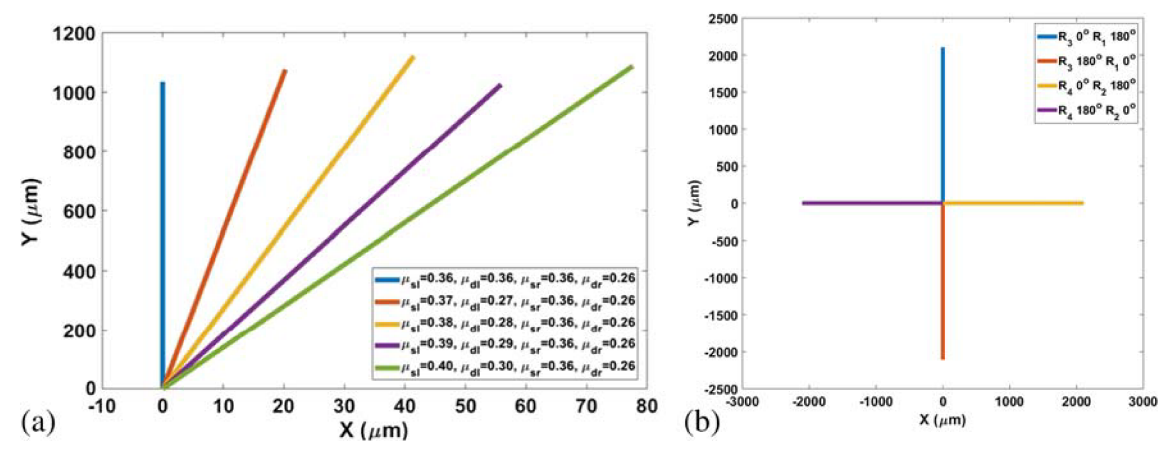


Fig. 8 (a) Result of SolarPede's motion trajectory simulation, with different friction constants on each leg. (b) Simulated trajectory of

Solar Pede's 2nd gaiting method. 180° phase shift between each combined actuation force

motion directions of the SolarPede, such as $\pm x$ and $\pm y$ and correspond to the direction of the arrows in Fig. 3.

If we break the assumption of "all four forces align with the center of mass," the microrobot would spin. In this case, the extension of the force does not pass through the center of mass, such as F_1' in Fig. 7. The distance from the center of the actuator to the center of mass denotes as r_x . Then the total moment of the body can be written as:

$$\sum M = I_M \ddot{\varphi} = r_1 \times F_1 + r_2 \times F_2 + r_3 \times F_3 + r_4 \times F_4 \#$$
 (7)

A moment I_M would cause spinning motion of the microrobot. If the fabrication and assembly were precisely done, the microrobot should not experience any torque. But due to fabrication and assembly imperfections, spinning motion may be generated. This effect can be caused by different contact conditions between the leg and the operating surface, or by damaged actuator beams, causing the leg to move along different directions than designed. Spinning motion of the SolarPede is desired if the microrobot will be used as a positioner. This effect was observed experimentally, as discussed in Section 5.3.

5 Experimental results

5.1 Experiment setup

Three aspects of the proposed design have been evaluated in the following sections: power efficiency, control methodology, and wirelessly powered payload motion validation. Three stages of experiments were conducted to evaluate the design. First, we prototyped the design with bread boards to validate the control method and evaluate efficiency of the boost converter; second, we integrated all electronic components and the MEMS die into one large scale circuit board, 7 cm in size, in order to evaluate the overall design. This PCB is shown in Fig. 9 (a). After this board was tested, we developed our first much smaller 2 cm size electronic backpack and wire bonded it to the MEMS die as shown in Fig. 9 (c).

The millimeter-size prototype validates the assembly of the SolarPede and evaluates the wireless powering capability. Components were selected from evaluation board experimental results. In this attempt to down-size the SolarPede, we mounted the solar cells on the power board shown in Fig. 1 (a). The voltage booster circuit was omitted due to efficiency

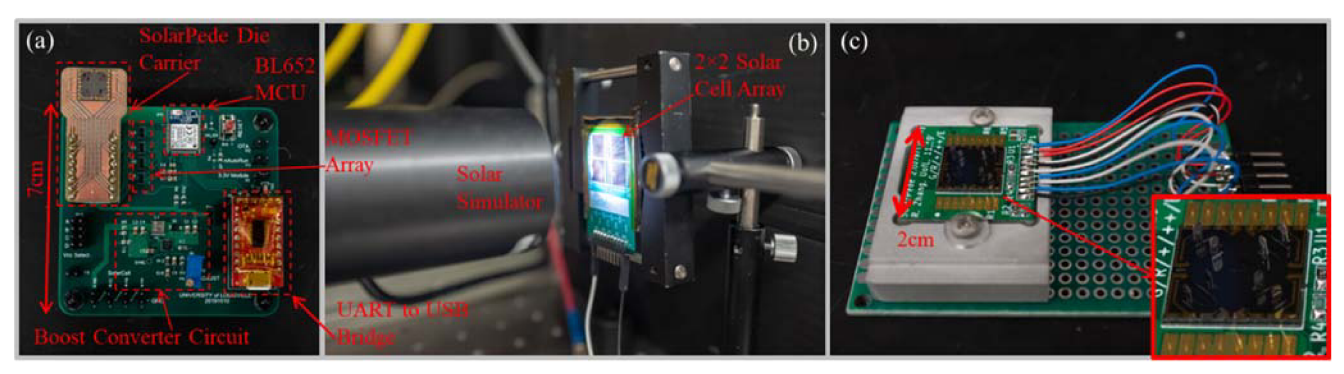


Fig. 9 (a) The 7 cm evaluation circuit. (b) Solar cell testing setup. (c) Millimeter-size prototype in a testing fixture

Table 1 Power consumption of a single thermal actuator from 5 to 20 V																
Voltage (V)	5	6	7	8	9	10	11	12	13	14	15	16	17	18	19	20
Current (mA)	12.4	14.5	17.5	20.7	23.7	26.0	28.1	30.2	31.5	33.2	34.4	35.7	36.5	37.1	37.8	38.4
Power (mW)	62	87	123	166	213	260	309	362	410	465	516	571	621	668	718	768

consideration. The Bluetooth module, the MOSFET array, and the actuator die were all installed on the control board. Insulated thin copper wires from the transformer can be used to connect the power and control boards and they can be adhered to each other.

To assist the wire bonding process of the MEMS device, a customized aluminum fixture with a machined cavity was made to hold the control board, so that the wire bonder has a flat and stable working surface. This setup also allows all ports on the control board, including UART and power, to be interfaced to test its functionality separately, as shown in Fig. 9 (c).

5.2 Power efficiency evaluation

Power is the most critical factor in SolarPede's electronics design, hence firstly evaluated. The power consumption of a single thermal actuator used in SolarPede was experimentally evaluated with stationary DC power supply. By swiping the voltage applied upon a single thermal actuator and measuring the current on the line, a power consumption curve was acquired, as shown in Table 1. As indicated from the experiment, with 10 V input, the thermal actuator consumes roughly 260 mW.

The solar cells used in our design must be small, highly efficient, and customizable, which lead us to the solar concentrator products from SpectroLab. The model we sampled was CDO-100 with 1 cm by 1 cm footprint. Four solar cells were assembled to a testing PCB, as shown in Fig. 9 (b). Another advantage of using this type of solar cell is that they can utilize above 1000 suns of concentrated irradiance [25] with proper cooling scheme, which allows us to increase power output from solar cells by increasing solar simulator power output.

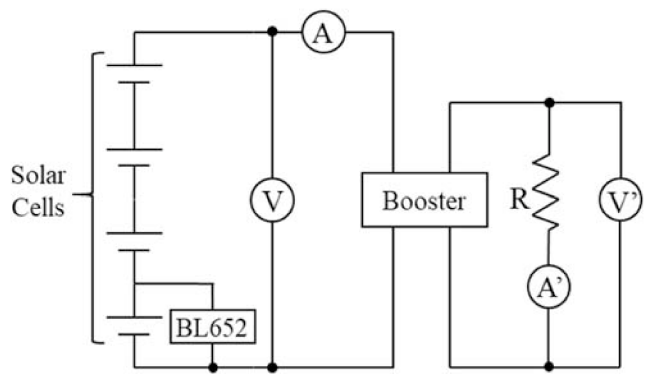
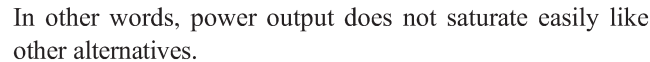


Fig. 10 Solar cell and booster efficiency evaluation experiment circuit schematic



The efficiency of the boost converter was measured from a group of experiments. Preliminary experiments suggest that a single cell could provide 2.5 V, 75 mW power under 5 suns of irradiance. As a result, we chose to use four cells in series as the power source to the SolarPede, because total of 10 V, 300 mW can power one actuator, and their weight can be balanced when mounted on top of the microrobot.

A circuit shown in Fig. 10 is used to determine the boost converter (TPS55340 from Texas Instruments®) circuit efficiency. V and A are the output voltage and current measured directly from the solar cells, R is the load – a single thermal actuator, and A' and V' are current passed through the load and the voltage across the load.

The efficiency of the booster is determined by the following equation:

Boosting Efficiency =
$$\frac{Load\ Power}{Solar\ Cell\ Power} = \frac{V^{'} \cdot A^{'}}{V \cdot A} \#$$
 (8)

Two constraints apply to such an experiment: 1) The input voltage to the TPS55340 should not be below 2.9 V. 2) If the output current A' cannot keep up with V', V' will drop below targeting voltage. For example, if we adjust the V' to 16 V, the thermal actuator requires 35.7 mA of current to maintain 16 V on the load. However, due to input power limitation, the boost converter cannot delivery 571 mW of power upon the load. At this moment, V' will drop below 10 V, which indicates the boosting fails. According to experiments, a reliable boosting voltage was determined at around 11.5 V. Under such condition, eq. (8) can be evaluated by the following measurements:



Fig. 11 Assembled and packaged SolarPede die carrying a payload



 Table 2
 Omnidirectional motion testing result

Direction of motion	Observed Displacement (over 10 s)	Observed Velocity
Up (+y)	155 μm	15.5 μm/s
Down (-y)	121 μm	12.1 μm/s
Left (-x)	133 μm	13.3 μm/s
Right (+x)	113 μm	11.3 μm/s
CW Rotation	_	3 mrad/s

Booster Efficiency =
$$\frac{V^{'} \cdot A^{'}}{V \cdot A} = \frac{11.2V \times 30.6mA}{10.0V \times 45.1mA} \approx \frac{342.7mW}{451.0mW} \approx 75.99\% \#$$
(9)

The efficiency of 75.99% matches datasheet specification. By using this configuration, 11.5 V can be reliably applied onto one actuator.

In order to use the limited power efficiently, we decided to remove the boost converter and apply 10 V directly on the actuators for the wirelessly powered operation, since 1.5 V voltage boost is not worth 24% power efficiency lost. This modification also reduces the weight of the backpack.

The Bluetooth MCU BL652 module consumes maximum 24 mW according to [22, 27], one tenth of a thermal actuator consumes, which can be easily covered by one solar cell and was confirmed by experiment.

5.3 Control method validation

The dynamic response of SolarPede's legs were investigated in [22], in which using a laser displacement sensor to validate the dynamic model in Section 4. Here, we conduct experiments to validate the functionality of our control methodology and circuit. The assembled SolarPede die was wire-bonded to a semiconductor carrier (Fig. 11) and connected to the rest of the circuit through wires. A stationary DC power supply was used to provide 30 V to power the actuators. In this test, the SolarPede was in a "belly-up" configuration: all eight legs were

Fig. 12 (a) Signals of second actuation method on actuator #1, #4, #2, and #3: amplitude modulation (AM) on top of half-period, 180° phase-shifted pulse-width modulation. Time between the two cursors is 20 ms, the PWM signal is 50% duty cycle, 500 Hz. (b) Illustration of overall signaling for method 2

facing upward, and a payload cut from a silicon wafer was placed directly onto the legs of SolarPede. This manner simulates the stick-and-slip motion of SolarPede without assembling the electronic backpack. To protect the integrity of the prototype, light payloads were used initially. The motion of the payload was recorded using a camera with 0.5, 0.6, and 1.2 g of weight. A scratch was made on the surface of the silicon payload to assist displacement evaluation. The payloads were tested in succession, having their motion recorded before switching to the next payload, which were increasingly heavy.

During experimentation, we decreased the duration of actuation pulse from 1 s, which allowed the human eyes to easily perceive the leg's motion and helped to troubleshoot errors in the gaiting patterns. By decreasing pulse duration to 100 ms, we observed that when each leg was actuated individually, the payload was not moving. If, however, the actuators were paired and moved in a synchronized manner, as described in method 3, the payload experiences a larger actuation force, and breaking static friction. In this manner, omnidirectional motion of the payload was achieved. The experimental results are presented in Table 2.

5.4 "Belly-up" payload motion testing powered by solar simulator

We tested our first millimeter-size prototype with the solar simulator (Newport 69,907, 67,005 and UXL-150S-O, Xe) to confirm that solar cell output is sufficient to drive the thermal actuators and hence move the payload under the "belly-up" configuration. In order to use the limited power from the solar cells efficiently, we can split the power to more than one actuator by 500 Hz pulse width modulation (PWM). On top of the PWM, an amplitude modulation (AM) defines individual actuation movement on each actuator.

However, this method only distributes power instead of generates more. According to our experiment, each thermal actuator consumes 260 mW of power under 10 V DC. In order to use method 1 mentioned in Section 2.2, four actuators powered simultaneously, 4×260 mW is required without PWM. If we use PWM with 50% duty cycle to power the four

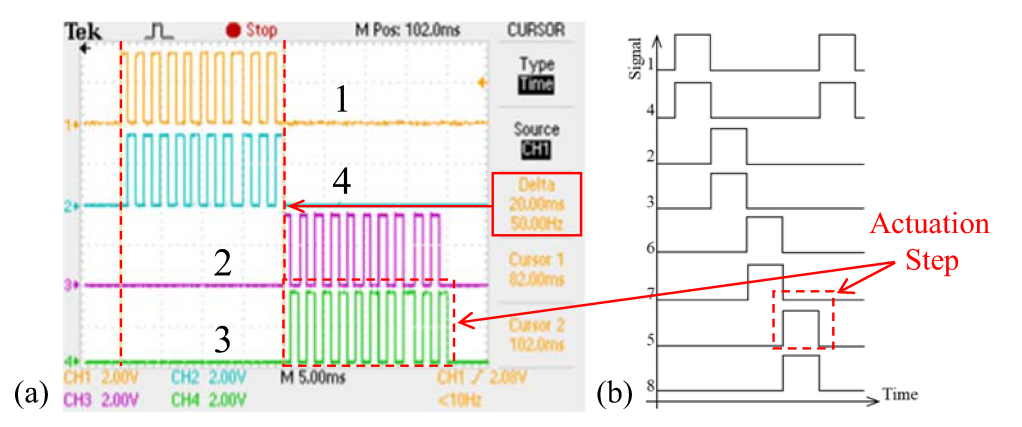




 Table 3
 Recorded payload displacement within 30s

Actuation Frequency (Hz)	100.0	71.4	50.0	25.0	16.7	12.5
Actuation Step Size (ms)	5	7	10	20	30	40
Total Displacement (µm)	1160	1178	1307	698	484	440
Velocity (µm/s)	38.67	39.27	43.57	23.27	16.13	14.67

actuators, the power consumption can be reduced to 2×260 mW, at the cost of reduced displacement. Applying the same powering scheme, method 2 can be driven by 260 mW with PWM signal and reduced motion. While method 3 powers one actuator at one time so it consumes 260 mW without the need of PWM. On the other hand, if the solar cells cannot keep up with the power consumption of the thermal actuators, the voltage output from the cells will drop below the typical value. In this case, the solar cells are not able to drive the thermal actuators anymore and motion ceases.

In order to balance power consumption and drive more legs, we use the 2nd actuation method introduced in Section 2.2 to conduct the experiment, which requires engaging two actuators simultaneously, such as actuators number 1 and 4. The two actuators can be powered by two PWM signals with 50% duty cycle each and half-period phase shifting, demonstrated in Fig. 12 (a). The next step of leg 2 and 3 are actuated by the same method. To generate force towards +y direction, the signal sequence shown in Fig. 12 (b) was implemented.

In this way, two actuators can be engaged at the same time (equivalent of driving one actuator) at the expense of reduced displacement. According to [15], the product of actuation frequency (f) and amplitude (A) positively correlates to the velocity of the motion. In our experiment, the actuation voltage amplitude was determined by the solar cell's voltage and the PWM duty cycle, but we have control over the length of the "on" time on each actuator,

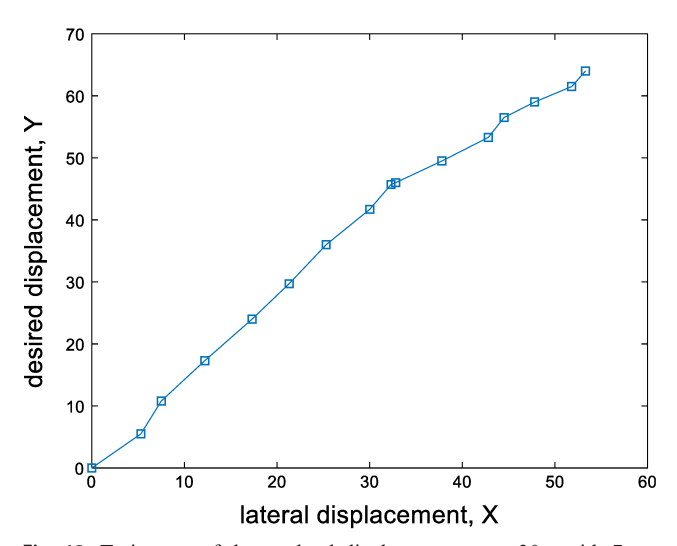
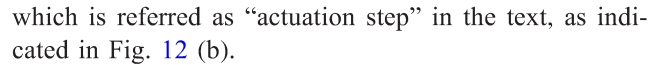


Fig. 13 Trajectory of the payload displacement over 30s, with 7 ms actuation step



In this experiment, the solar cells were exposed under 8 suns (790 mW/cm²) of irradiance, and about 400 mW were measured from the solar cells. A piece of single-side-polished Silicon die weigh 0.1 g was used as the payload, by applying sequence from method 2, displacement of the payload over 30s was recorded by a camera. Results are collected in Table 3. However, if we increase the payload to 0.4 g the motion ceases, possibly due to limited power. Therefore, in future refinements of the SolarPede design, the microrobot weight must decrease from 4 g to a much smaller number, the locomotion mechanism must be improved, or the light power must be boosted.

Figure 6 indicates that robot velocity is expected to increase if actuator voltage increases, and decreases, respectively, if the actuation frequency increases. With SolarPede, we are limited to around 10 V supply from the solar cells. As a result, the model predicts that velocity will be mostly constant between 5 and 10 µm/s as we sweep leg actuation frequencies from 10 Hz to 100 Hz. Experiments suggest that while this trend may be true at low frequencies, with recorded velocities around 15 µm/s, we also observed that payload displacement was maximized at frequencies closer to 50 Hz. Indeed, velocities closer to 40 µm/s were observed for frequencies below 100 Hz, suggesting that higher velocities can be obtained at higher leg actuation frequencies. This effect is not captured by the dynamic model shown in Fig. 6 (b), possibly due to ignoring additional effects such as vertical leg and joint flexibility that may be resonating at higher frequencies. In our past work with ARRIPede [10], the robot velocity was correlated with the square of the amplitude-frequency product, and our current observations are consistent with that conclusion.

Figure 13 shows the payload's trajectory within 30s, in which the desired displacement direction was the +Y axis. However, an undesired lateral displacement along X axis occurred, which can be explained by unbalanced friction forces on the lateral directions. Furthermore, small tilts on the legs during assembly could cause uneven friction force distribution, further leading to the lateral motion of the microrobot.

6 Conclusion and future work

In this paper we present analysis and experimental results that validate the untethered operation of SolarPede as a novel light-powered micro-crawler. The microrobot body was fabricated using DRIE process from SOI wafers with 1 cm² footprint. 8 Silicon legs were assembled into compliant socket connectors using a custom microassembly station in our lab. The leg layout on the microrobot body ensured that omni-directional 2D motions can be achieved using stick-and-slip of the leg to the



operating surface. An electronic backpack consisting of a Bluetooth enabled microcontroller, four solar cells, and power electronics was designed and connected to the packaged body of the microrobot. A stick-and-slip model was implemented to analyze leg displacement as well as expected force output. Further, the model was used to predict the microrobot's motion velocity and trajectory. The locomotion of the microrobot was studied in the "belly-up" or conveyor configuration by placing a payload on top of the inverted legs. Experiments were conducted to verify that the robot can achieve translational motions upon up-down and left-right directions; under solar cells powered trials, a maximum speed of 40 $\mu m/s$ can be achieved with 8 suns of artificial light irradiation.

In future work, dynamic simulations will be conducted to optimize additional design aspects of the SolarPede. New leg designs, placement and numbers will be investigated for handling of assembly errors, heavier payload, and traversing different surface materials and flatness conditions. The size and weight of the electronics backpack will be further decreased and SolarPede microrobot can be fully tested. Furthermore, closed-loop control of the planar position of the microrobot will be achieved using visual microscope feedback to affect the gait cycles in appropriate quadrants and correct for undesired drift motions.

Acknowledgements This work was supported by National Science Foundation Grants #IIS 1633119 and #CMMI 1734383. We wish to thank the Micro Nano Technology Center (MNTC) staff at the University of Louisville, for their help with cleanroom fabrication and wire bonding. We also wish to thank Douglas Jackson, for his dedicated help on the PCB designing and assembly.

References

- Tanaka M (2001) Development of desktop machining microfactory. In: RIKEN Review: Focused on Advances on Micro-mechanical Fabrication Techniques, no. 34, pp. 46–49
- Zhakypov Z, Uzunovic T, Nergiz AO, Baran EA, Golubovic E, Sabanovic A (2014) Desktop microfactory for high precision assembly and machining. In: IEEE 23rd International Symposium on Industrial Electronics (ISIE). Istanbul, Turkey
- Diederichs C, Mikczinski M, Tiemerding T (2014) A flexible and compact high precision micro-factory for low volume production and lab-automation. In: 41st International Symposium on Robotics. Munich, Germany
- Zhakypov Z, Uzunovic T, Nergiz AO, Baran EA, Golubovic E, Sabanovic A (2017) Modular and reconfigurable desktop microfactory for high precision manufacturing. Int J Adv Manuf Technol 90(9–12):3749–3759
- Murthy R, Popa DO (2010) Millimeter-scale microrobots for waferlevel factories. In: IEEE International Conference on Robotics and Automation. Anchorage, AK, USA
- Hsu A, Cowan C, Chu W, McCoy B, Wong-Foy A, Pelrine R, Velez C, Arnold D, Lake J, Ballard J, Randall J (2017) Automated 2D

- micro-assembly using diamagnetically levitated milli-robots. In: International Conference on Manipulation, Automation and Robotics at Small Scales (MARSS). Montreal, QC, Canada
- Pelrine R, Wong-Foy A, Hsu A, McCoy B (2016) Self-assembly of milli-scale robotic manipulators: a path to highly adaptive, robust automation systems. In: International Conference on Manipulation, Automation and Robotics at Small Scales (MARSS). France, Paris
- Zhang J, Onaizah O, Middleton K, You L, Diller E (2017) Mobile magnetic microgripper for autonomous pick-and-place. IEEE Robot Autom Lett\ 2(2):835–840
- Murthy R, Das AN, Popa DO (2009) Nonholonomic control for an assembled microcrawler. IFAC Proc 42(16):627–632
- Murthy R, Das AN, Popa DO, Stephanou HE (2011) ARRIpede: an assembled die-scale microcrawler. Adv Robot 25(8):965–990
- Pelrine R, Hsu A, Cowan C, Wong-Foy A (2017) Multi-agent systems using diamagnetic micro manipulation from floating swarms to mobile sensors. In: International Conference on Manipulation, Automation and Robotics at Small Scales (MARSS). Montreal, Canada
- Woern H, Szymanski M, Seyfried J (2006) The I-SWARM project.
 In: The 15th IEEE International Symposium on Robot and Human Interactive Communication. Hatfield, UK
- Shroff SS, de Boer MP (2015) Constant velocity high force microactuator for stick-slip testing of micromachined interfaces. J Microelectromech Syst 24(6):1868–1877
- Jafferis NT, Helbling EF, Karpelson M, Wood RJ (2019) Untethered flight of an insect-sized flapping-wing microscale aerial vehicle. Nature 570:491–495
- Murthy R, Das A, Popa DO (2008) ARRIpede: a stick-slip micro crawler/conveyor robot constructed via 2 ½D MEMS assembly. In: IEEE/RSJ International Conference on Intelligent Robots and Systems. Nice, France
- Geisberger A, Skidmore G, Tsui K (2004) Microconnectors and non-powered microassembly therewith. United States Patent EP1564183A2, 13 2
- Murthy R, Stephanou HE, Popa DO (2013) AFAM: an articulated four axes microrobot for nanoscale applications. IEEE Trans Autom Sci Eng 10(2):276–284
- Fahlbusch S, Fatikow S, Seyfried J, Buerkle A (1999) Flexible microrobotic system MINIMAN: design, actuation principle and control. In: IEEE/ASME International Conference on Advanced Intelligent Mechatronics. Atlanta, GA, USA
- Breguet JM, Clavel R (1998) Stick and slip actuators: design, control, performances and applications. In: International Symposium on Micromechatronics and Human Science. Nagoya, Japan
- Que L, Park J-S, Gianchandani YB (2001) Bent-beam electrothermal actuators-part I: single beam and cascaded devices. J Microelectromech Syst 10(2):247–254
- Park J-S, Chu LL, Oliver AD, Gianchandani YB (2001) Bent-beam electrothermal actuators-part II: linear and rotary microengines. J Microelectromech Syst 10(2):255–262
- Zhang R, Wei D, Popa DO (2018) Design, analysis and fabrication of sAFAM, a 4 DoF assembled microrobot. In: International Conference on Manipulation, Automation and Robotics at Small Scales (MARSS). Nagoya, Japan
- Yang Z, Saadatzi MN, Zhang R, Sherehiy A, Wei D, Harnett KC, Popa DO (2019) Multiphysics dynamic model validation methodology for laser-driven microrobots. In: 2019 IEEE 15th International Conference on Automation Science and Engineering, Vancouver
- Klotz JF, Wei D, Yang Z, Zhang R, Sherehiy A, Saadatzi MN, Popa DO (2019) Concept validation for a novel stick-and-slip, lightpowered, Mobile micro-crawler. In: 2019 International Conference on Manipulation, Automation and Robotics at Small Scales (MARSS). Helsinki, Finland



- Spectrolab I (2020) Concentrator Cells. SPECTROLAB, INC, 22 2.
 [Online]. Available: http://www.spectrolab.com/photovoltaics. html#concentrator. [Accessed 22 2 2020]
- Das AN, Zhang P, Lee WH, Popa D, Stephanou H (2007) µ3: multiscale, deterministic micro-Nano assembly system for construction of on-wafer microrobots. In: IEEE International Conference on Robotics and Automation. Roma, Italy
- Laird Connectivity (2019) BL652 Series Bluetooth v5 + NFC," 29
 [Online]. Available: https://connectivity-staging.s3.us-east-2. amazonaws.com/2019-05/CS-DS-BL652%20v2_9.pdf. [Accessed 10 2 2020]

Publisher's Note Springer Nature remains neutral with regard to jurisdictional claims in published maps and institutional affiliations.

